

Tandem bulk oxygen diffusion and surface reactions in reducible metal oxides control redox cycle dynamics

Received: 28 November 2025

Accepted: 27 March 2026

Cite this article as: Kim, Q., Yan, G., Worrada, A. *et al.* Tandem bulk oxygen diffusion and surface reactions in reducible metal oxides control redox cycle dynamics. *Nat Commun* (2026). <https://doi.org/10.1038/s41467-026-71787-0>

Quentin Kim, George Yan, Alfred Worrada, Sanjana Srinivas, Sinmyung Yoon, Sagar Sourav, J. Anibal Boscoboinik, Weiqing Zheng & Dionisios G. Vlachos

We are providing an unedited version of this manuscript to give early access to its findings. Before final publication, the manuscript will undergo further editing. Please note there may be errors present which affect the content, and all legal disclaimers apply.

If this paper is publishing under a Transparent Peer Review model then Peer Review reports will publish with the final article.

Tandem Bulk Oxygen Diffusion and Surface Reactions in Reducible Metal Oxides Control Redox Cycle Dynamics

Quentin Kim^{1,2,*}, George Yan^{2,*}, Alfred Worrad^{1,2,*}, Sanjana Srinivas^{1,2,*}, Sinmyung Yoon², Sagar Sourav^{2,3}, J. Anibal Boscoboinik⁴, Weiqing Zheng², Dionisios G. Vlachos^{1,2,#}

¹ Department of Chemical and Biomolecular Engineering, University of Delaware, Newark, DE 19716, United States

² Delaware Energy Institute, University of Delaware, Newark, DE 19716, United States

³ Department of Chemical Engineering, Indian Institute of Technology Madras, Chennai, Tamil Nadu 600036, India

⁴ Center for Functional Nanomaterials, Brookhaven National Laboratory, Upton, NY 11973, USA

To whom correspondence should be addressed. Email: vlachos@udel.edu

* These authors contributed equally

Abstract

The interplay between bulk oxygen diffusion and surface reactions in reducible metal oxides is key in heterogeneous catalysts, but direct measurements of oxygen mobility, transient kinetics, and *in situ* spectroscopies have been lacking. Here, we reveal complex dynamic behavior of ceria-zirconia by H₂ using transient kinetics via mass spectrometry and *in situ* Raman and near-ambient pressure x-ray photoelectron spectroscopies. Molecular dynamics simulations with a machine learning potential delineate competitive oxygen diffusion mechanisms, with an optimal mobility at intermediate reductions. We expose a compensation between vacancy availability and lattice distortion at intermediate to high reductions and Frenkel defects at low reductions, underscoring a potential deficiency of ¹⁶O/¹⁸O exchange experiments in deducing oxygen mobility. Vacancies in proximity require electron localization on Ce atoms further away. The continuous replenishment of surface oxygen results in a varying reduction rate, with H₂ dissociation being the rate-limiting step. Multiscale transient simulations, consistent with experiments, indicate catalysts of potentially spatially varying oxidation states. The approach is broadly applicable to reducible oxide materials.

Introduction

The versatile chemistry of reducible metal oxides enables their application in many thermochemical processes. Ceria-based materials are ubiquitous in heterogeneous catalysis, owing to their highly reactive surface oxygen (vacancies), tunable composition, and flexible environment-dependent surface chemistry.¹ Their catalytic applications include CO and hydrocarbon oxidation, which leverage the reactive surface oxygen; redox reactions, such as water-gas shift and methane reforming, which leverage the oxygen vacancies; and organic reactions, which leverage the tunable surface acidic and basic sites.^{2,3} The high oxygen storage capacity and thermal stability of doped cerias uniquely qualify them as an oxygen conductor in solid oxide fuel cells and an oxygen (vacancy, V_O)-storage medium for oxidation and reduction reactions in thermochemical looping in newer applications.^{4,5} The rapid temperature response of emerging electrified reactors facilitates transient processes, such as chemical-looping water-splitting and methane reforming, where lanthanide-doped cerias and Ce/Zr mixed oxides (CZO) have been demonstrated as active materials.^{6,7} Ultimately, the design and optimization of these novel reactors for hydrocarbon processing require an understanding of material property and reactivity across the atomic and continuum scales and in variable reaction regimes.

Redox reactions over ceria-based catalysts often follow (reverse) Mars-van Krevelen (MvK)-type mechanisms, involving reactant oxidation by lattice oxygen and the replenishment of oxygen vacancies by a soft oxidant. Despite the popularity of ceria-based catalysts, the kinetic behavior of MvK-type mechanisms, especially regarding the roles of surface and bulk oxygen, is a topic of debate.⁸ Although oxidation and reduction elementary steps involve both oxygen species, surface properties have typically been the focus of kinetic and mechanistic studies. The high sensitivity of ceria-based materials to oxidizing and reducing environmental conditions necessitates the use of *in situ* and *operando* techniques for surface and bulk characterization. Presently, the role of bulk oxygen is addressed through reactor studies in top-down approaches by measuring the rates of oxygen removal reactions at differing degrees of overall reduction and by isotope exchange experiments.⁹⁻¹²

Detailed modeling of bulk and surface properties of ceria-based materials eludes conventional computational methods. Although the high diffusivity of oxygen in ceria-based materials is well-known, modeling the mobility of bulk oxygen requires multitude of dynamical phenomena. At high temperatures, the distortion of the lattice structure due to reduction, the diffusion of oxygen

in conjunction with polaron hopping, and the collective and/or off-lattice motion of atoms all influence bulk oxygen mobility.¹³⁻¹⁶ Although these effects can be captured by ab-initio molecular dynamics (AIMD), the (relatively) costly density functional theory (DFT)-based electronic structure calculations hinder the exploration of phenomena beyond the picosecond timescale. On the other hand, the limited accuracy of conventional DFT methods for the prediction of the energetics of surface redox reactions presents a further challenge for building kinetic models from first-principles.^{17,18}

Here, we combine experimental kinetic and spectroscopic measurements, molecular simulations, and multiscale modeling to develop an atomistic understanding of ceria-based materials' reduction. CZO was reduced while monitoring the extent of reduction and the possible origin of the removed oxygen. The reduction experiments were paired with *in situ* spectroscopic measurements to provide further insights into the reduction process. Molecular dynamics (MD) simulations based on a machine learning potential (MLPs) trained on DFT calculations uncover nanosecond-scale spatiotemporal dynamics of lattice oxygen and unbiasedly address their mobility at experimentally relevant temperatures and degrees of overall reduction. Finally, joint experimental/computational transient kinetic studies resolve the mechanism of CZO reduction and quantify the roles of surface reaction and surface/bulk oxygen exchange.

Results

Kinetic and Spectroscopic Observations of CZO Reduction

The H₂ temperature programmed reduction (TPR) spectrum of CZO has two peaks around 545 and 700 °C that are commonly associated with surface reduction and bulk reduction, respectively (Figure 1a).¹⁹ The 545 °C peak corresponds to 1125 μmol/g, so lattice O (O_L) is removed from at least the outer 66% mantle of the CZO particle, indicating that, unlike typical literature assignments, O diffusion from the bulk to the surface significantly contributes to the first peak. Higher temperatures enable further reduction; the peak at 700 °C accounts for the remaining 502 μmol/g of removed O. By 800 °C, a total of 1627 μmol/g of O has been removed, and the CZO is reduced to an extent of reduction (ξ_{red} , see Methods and Section S1) of 0.96. Clearly, labeling the two peaks as surface and bulk reduction is an oversimplification, as the majority of the CZO reduction occurs in the 545 °C peak. In fact, within the first peak, the quantity equivalent to all

removable surface O (“first monolayer” in Figure 1a) has already been removed by 396 °C, long before the maximum.

To assess the kinetics of CZO reduction at various temperatures, we reduced the CZO isothermally by flowing H₂ and monitored ζ_{red} (Figure 1b). At 500 °C, the H₂O formation rate starts at a maximum and gradually declines (a sharp initial rise due to reactor startup was omitted here for brevity). This unexpected behavior reflects the combined dynamics of surface reaction with H₂ and bulk O (O_b) diffusion, which replenishes surface vacancies (V_O). While various surface and mass transfer effects can affect H₂O formation, the H₂O generated during reduction exceeds the estimated amount of removable surface O (O_s), which is calculated from the particle surface area and O surface density (Eq. S2). This indicates that the particle surface would rapidly become O deficient without continuous replenishment from the bulk (Eq. S5). Specifically, at a constant H₂ flow, one would expect the H₂O rate to decrease continuously with time as O_s declines. Upon removing O from the surface layer, the rate may drop further due to diffusion limitations, with a square root dependence on time, as indicated by textbook analysis of the diffusion equation. The rate normalized by the number of removable O_s, $N_O^s(t)$, determined from an overall O balance and the H₂O detected via mass spectrometry (MS), should reflect the intrinsic rate constant of O_L removal and remain static. However, the data (Figure 1b) indicates a continuous decline in the normalized rate of H₂O formation (k_{H_2O}) with time on stream or ζ_{red} . k_{H_2O} can be calculated by assuming either surface reaction limitations or bulk diffusion limitations, but assuming diffusion limitations produces unphysical values of k_{H_2O} (Methods and Section S1).

To probe the relation between bulk and surface oxygens, we characterized the reduction of CZO using *in situ* Raman spectroscopy, leveraging its moderate surface sensitivity. Upon reduction of the CZO, the longitudinal optic (2LO) mode at 1200 cm⁻¹ decreases in intensity while the feature at 2110 cm⁻¹, corresponding to an electronic transition of Ce³⁺, increases in intensity (Figure S2a).^{7,20-22} Interestingly, the 2LO overtone and Ce³⁺ features coexist when CZO is partially reduced, reflecting a balance between oxidized and reduced states. When the gas flow alternates between 10% H₂/Ar and pure Ar, the CZO appears to reoxidize despite the lack of inlet oxidant flow (Figure S2b). This suggests that O diffusion from the bulk to the surface replenishes surface V_O, and that the delay in oxidation observed by Raman may reflect diffusion limitations. However, the lasers in Raman spectroscopy may penetrate hundreds of nanometers deep into the sample, although this is dependent on factors including, but not limited to, sample condition and laser

wavelength.²³⁻²⁵ A CZO particle is approximately 32 nm in diameter (see XRD and BET analyses in Section S1), so the Raman laser is capable of penetrating entire CZO particles and potentially lacking surface sensitivity. Additionally, CZO absorbance increases as it reduces, changing penetration depth and Raman scattering intensity at the affected vibrational modes (2110 cm^{-1}) due to the resonance Raman effect (Figure S2c). A control experiment with inert SiO_2 instead of CZO also shows that H_2 remains in the cell during the Ar purge, and the residual H_2 could explain the delay in oxidation observed by Raman (Figure S3). The observed dead volume and possible temperature inhomogeneities can make *in situ* spectroscopy cells unsuitable for direct comparison to the reactors used in kinetic studies; criteria for *operando* cells and designs were explored in other works.²⁶⁻²⁸ A preliminary kinetic analysis can help determine whether diffusion barriers are present and if they are discernible within the spatiotemporal limitations of Raman spectroscopy.

In analyses of particle diffusion processes, two extreme cases are often employed (see discussion in Section S1). In the fast diffusion limit, the mobile species diffuses through the bulk faster than the characteristic time scales of surface reactions to keep up with surface transformation, and the bulk concentration profile is flat. In the slow diffusion limit, surface reactions are much faster and instantly consume species arriving from the bulk, inducing significant bulk concentration gradients. Previous works have effectively demonstrated that O_L diffusion in CZO is faster than the surface reduction reaction, but they rely on indirect kinetic measurements without direct probing of O_L concentrations within CZO particles.^{9,10} Techniques such as electron energy loss spectroscopy²⁹ or x-ray photoelectron spectroscopy (angle-resolved, depth profiling)^{30,31} can directly measure Ce^{3+} and O_L concentrations, but these characterizations are rarely performed at relevant reaction conditions and lack the spatial and temporal resolution to track O_b diffusion. Monitoring CZO reduction using near ambient pressure x-ray photoelectron spectroscopy (NAP-XPS) resulted in qualitatively similar results to *in situ* Raman spectroscopy; though, the results are not sufficient for diffusion analyses. The operating pressure of 1 mbar H_2 is still far from typical reaction conditions, and although there is good time resolution, this set of data has no depth resolution, the addition of which would prevent effective time resolution (Figure S4). We instead turn to computational methods to fill in the gaps beneath the surface.

Molecular Simulations of Bulk Oxygen Mobility

The multiple possible mechanistic hypotheses regarding the role of O_b , which may form based on kinetic and spectroscopic observations, raise questions regarding its mobility under reaction

conditions. To understand how temperature and V_O concentration influence the self-diffusivity of O in the CZO bulk, we performed MD simulations at five ζ_{red} levels: 0.06, 0.13, 0.25, 0.38, and 0.50, corresponding to the presence of 4, 8, 16, 24, and 32 V_O in the simulation cell, respectively (Methods). Simulations spanned temperatures of 1100-1500 °C to enable sufficient sampling of O diffusion rare events. Figure 2a presents the activation energies (E_a) and pre-exponential factors (D_o) extracted from Arrhenius fits, $D = D_o \exp(-E_a/RT)$, at each ζ_{red} . When $\zeta_{red} \leq 0.25$, E_a depends weakly on ζ_{red} , and D_o is also relatively constant. The substantial increase of both E_a and D_o at higher ζ_{red} is reminiscent of the compensation effect; though, overall, the variations indicate a complex relationship between ζ_{red} and diffusivity. These sharp nonlinearities also reveal a deficiency in using the rate of $^{16}O/^{18}O$ exchange as an indicator of O_b mobility: since the measurements must be made under oxidant-rich environments, the inferred diffusivity only corresponds to that in the low ζ_{red} regime where diffusion proceeds through Frenkel defects. To more clearly resolve the dependence of diffusivity on ζ_{red} at a fixed temperature, we performed additional simulations at intermediate reductions at 1200 °C. As shown in Figure 2b, the diffusivity exhibits a clear power-law dependence on ζ_{red} , with a best-fit in the form of $D = A \zeta_{red}^B = 1.2 \times 10^{-6} \zeta_{red}^{0.72} \text{ cm}^2/\text{s}$. It is important to note that this expression is temperature-dependent due to the variation of D_o and E_a for each reduction. At 1200 °C, the behavior is autocatalytic: the more vacancies, the faster the diffusion.

Building on these observations, we used the complete set of Arrhenius parameters to construct a diffusivity heat map across the entire temperature range of interest (Figure S12) as well as the estimated diffusion timescales for a spherical CZO particle 30 nm in diameter (Figure 2c). The heat map reveals a maximum for our operating conditions of 600 °C at $\zeta_{red} = 0.25$. Note that a volcano-type dependence of O_L diffusivity on the overall degree of reduction was recently reported based on a regression of the rate of re-oxidation reactions measured in the bulk diffusion-limited kinetic regime.³² The maximum at intermediate ζ_{red} most likely arises from competing effects. At low ζ_{red} (below ~ 0.1), diffusion is limited by the lack of vacant sites, while at higher ζ_{red} (above 0.35), lattice distortions increase the energy barrier for diffusion. This distortion is visible in the O-O radial distribution functions (g_{OO}) and top-view structures shown in Figure 2d, where an increased density appears between the first and second coordination shells at $\zeta_{red} = 0.5$ compared to the pristine case. The broadening of intermediate range order is accompanied by the expected diminished first peak, indicating a disruption of the well-defined local structure. Together, these

features are consistent with increased lattice distortion supporting the notion that significant structural disorder occurs at higher vacancy concentrations. The resulting compensation effect between site availability and lattice distortion governs the mechanism of diffusion at intermediate to high ζ_{red} , where Frenkel defects play less of a role.

To further understand the mechanism of O_b diffusion, we analyzed the MD trajectories in detail, focusing on the dynamics of V_O . We identified the initial positions of V_O by locating vacant O sites (tetrahedral interstitials) in the initial frame. To construct a trajectory for V_O , we track the O atoms that move into vacant sites, effectively treating V_O as if they had moved in the opposite direction. The plot (Figure S13) shows the cross-correlation of V_O 's velocities as a function of pairwise distance, with distances binned into coordination shells that align with the major peaks in g_{OO} . We use the absolute value of velocity components to capture co-directional motion along the same Cartesian axis. The correlated V_O mobility is minimal in the first coordination shell (0-3.25 Å) and reaches its maximum in the third shell (5-6.75 Å). The third shell corresponds to intermediate V_O separations, with every other lattice site occupied by O in each direction. For the second coordination shell (3.25-5 Å), a moderate correlation is observed at all correlation times, with a maximum at the initial time, indicating brief coordinated motion of closely spaced V_O . The decay of the second shell correlation at short times indicates a tendency for V_O to move away from one another. Overall, the correlated V_O mobility corroborates a uniform distribution of V_O in a maximally reduced system ($Ce_{0.5}Zr_{0.5}O_{1.75}$), as clusters of V_O are less energetically favorable. V_O in proximity require electron localization on Ce atoms further away, due to the unfavorable nature of Ce^{2+} sites. These results indicate that enhanced diffusion occurs at intermediate V_O concentrations, which favor spacing for V_O migration.

Multimodal Kinetic and Mechanistic Investigations of CZO Reduction

With an understanding of the diffusivity of O_b across a broad range of temperatures and ζ_{red} , we return to explore the mechanism of CZO reduction. We first assess the appropriateness of calculating k_{H_2O} in the fast diffusion limit, akin to the traditional turnover frequency definition of the catalytic rate. Using the radius of a CZO particle from BET analysis (16 nm) as the characteristic length scale and a diffusivity of 10^{-9} cm²/s (Figure S12), the diffusion timescale, $\tau_{diff} = \frac{L^2}{D}$, is ~ 0.003 s, while the reaction timescale, $\tau_{rxn} = \frac{1}{k_{H_2O}(t=0)}$, is ~ 40 s, at least four orders of magnitude higher and further exacerbated as diffusivity increases with CZO reduction up to a

maximum (Figure 2c and S12). The analysis of k_{H_2O} in the fast-diffusion limit is well-justified, corroborating with the kinetic analysis evaluated independently from the molecular simulations (Section S1).

Reduction experiments conducted with different H_2 partial pressures and at different temperatures reveal insights into reduction kinetics and surface species behavior. Based on the value of k_{H_2O} at various ξ_{red} and their maxima (k_{max}), H_2 pressure has a reaction order of 0.88 ± 0.05 (Figure 3a and S5a). A reaction order close to one indicates H_2 dissociation is likely the rate-determining step. On the other hand, Arrhenius relations constructed using k_{H_2O} at various ξ_{red} and k_{max} shows that the E_a of CZO reduction is 99 ± 8 kJ/mol (Figure 3b and S5b). Unexpectedly, k_{H_2O} does not remain constant during reduction. There is an initial inflection in k_{H_2O} , which is more gradual at higher temperatures, followed by a maximum and a drop that is more pronounced at 450 °C.

To understand the mechanism of CZO reduction at the atomistic level, we studied the dissociation of H_2 and the removal of surface O using DFT calculations. Specifically, we considered the (111) facet of CZO as it was previously determined to be the most stable one.³³ Surface reduction initiates through the heterolytic dissociation of H_2 across a surface Zr-O_{Zr,s} bond, facilitated by the stronger Lewis acidity of the surface Zr⁴⁺ cation compared to Ce⁴⁺ [See Figure S14 for site nomenclature and Figure S15 for intermediates (IS) and transition states (TS)]. Following dissociation, the H atop Zr can migrate to a nearby O, reducing two surface Ce⁴⁺ to Ce³⁺. Two migration pathways were explored; the first (direct) pathway was the migration to subsurface O_{Ce,ss}, which elevates O_{Ce,ss} close to the surface and forms a H-O_{Ce,ss} + H-O_{Zr,s} pair. This pair is strongly stabilized by hydrogen bonding, and its decomposition to H₂O and O_{Ce,ss} occurs barrierlessly. Finally, the chemisorbed H₂O desorbs to create an O_{Zr,s} vacancy, V_{O,Zr,s}, completing the O_{Zr,s} + H₂ → V_{O,Zr,s} + H₂O redox half-cycle. The alternative pathway is the migration of H to O_{Zr,s}, with a similar barrier as that of the direct pathway. Although the produced H-O_{Zr,s} + H-O_{Zr,s} pair does not involve H bonding, it is more stable than H-O_{Ce,ss} + H-O_{Zr,s}, which can be subsequently formed by crossing a small barrier.

To account for the influence of experimental conditions on the surface reduction energetics, we constructed a pressure-corrected free energy diagram (Figure 4a). Under a representative environment ($T = 500$ °C, $P_{H_2} = 10^{-1}$ atm, and $P_{H_2O} = 10^{-2}$ atm), the initial surface reduction of

CZO clearly follows two macroscopic timescales, corresponding to the dissociation of H₂ and the desorption of H₂O. These timescales are controlled by the stability of the H migration TS, of the H-O_{Zr,s} pair product, of the TS of H₂O desorption (see Section S4 and ref³⁴), and of the V_{O,Zr,s} product. Further refinement of the energetics of key states through single point calculations at the HSE06+D3BJ level (red and blue markers in Figure 4 representing the use of 25% and 15% exact exchange, respectively) reveals that the initial H₂ activation sequence is the most kinetically relevant, as the net free energy barrier relative to gaseous H₂ is much higher than that from the H-O_{Zr,s} + H-O_{Zr,s} pair to the TS of H₂O desorption.

Although the kinetics of the initial surface reduction can be deduced from the free energy diagram, the role of O_b is not yet clear. Since the self-diffusion of O_b occurs rapidly (Figure S12), the O concentration profile in the particle interior should be uniform, and the catalyst's response should be controlled by surface reduction reactions.^{9,10} Indeed, considering a diffusivity of $\sim 10^{-9}$ cm²/s and an O-O site spacing of ~ 2.5 Å, one estimates the O/V_O hopping frequency to be $\sim 10^7$ s⁻¹. This effective single-event rate constant far exceeds that of H₂ dissociation. To capture the multiscale (simultaneous surface and bulk) reduction of a CZO nanoparticle, we developed a model treating the surface and a uniform bulk as distinct phases in equilibrium (see Section S4, Figure S16 and Eq. S6-S22).

Isothermal kinetic simulations of a single CZO particle reveal that the reduction of CZO occurs at a timescale of minutes and depends positively on P_{H_2} (Figure 5b and Figure S17). At $T = 500$ °C, $P_{H_2} = 10^{-1}$ atm, and $P_{H_2O} = 10^{-2}$ atm, the single-particle $k_{H_2O}^p$ ($k_{H_2O}^p$, see Eq. S21 and S22) reaches a maximum of 0.05 s⁻¹ after the rapid quasi-equilibration of H₂O desorption (Figure S18). In line with the free energy pathway, H₂ dissociation is clearly the rate-determining process: the elementary step is always far from quasi-equilibrium, and the maximum $k_{H_2O}^p$ (k_{max}^p) depends linearly on P_{H_2} (Figure S19), in agreement with experimental measurements. Appreciable formation of V_O begins at ~ 10 s, where the removal of O_{Zr,s} and O_b occur simultaneously, in agreement with spectroscopic observations. As more V_O form over the course of reduction, the coverage of HO_{Zr,s} gradually grows as it is controlled by P_{H_2O} and the re-adsorption of H₂O on V_O; nevertheless, it remains low (Figure 5b). A greater P_{H_2O} results in a decline in k_{max}^p (Figure S20). For the bimolecular H₂ activation process (heterolytic dissociation to a homolytic product), as O_L is gradually removed, $k_{H_2O}^p$ slowly declines as fewer O_{Zr,s} sites remain to react with H₂. Despite

the amount of O_L removed already exceeding $\frac{1}{4}$ of $O_{Zr,s}$ sites (removable surface O; see Section S4) by 21 s, $k_{H_2O}^p$ only slightly diminishes due O_b continuously replenishing $O_{Zr,s}$. Like at 500 °C, $k_{H_2O}^p$ at 450 and 600 °C also quickly reaches k_{max}^p early on and only slowly decays (Figure 5c). At constant P_{H_2} and P_{H_2O} , the coverage of $HO_{Zr,s}$ decreases with temperature, as H_2O re-adsorption becomes progressively endergonic (Figure 5c). Based on the calculated k_{max}^p , we estimate an E_a of 101 kJ/mol (Figure S19b), in agreement with the experimentally measured 99 kJ/mol (Figure S5).

With a working model of isothermal reduction kinetics in hand, we revisit the temperature programmed reduction (TPR) of a single CZO particle. When the free energy change of the bulk/surface O exchange (ΔG_{O°) was set to 0 eV (same as that in isothermal reduction simulations), a single H_2O formation peak was observed at 542 °C, in agreement with experimentally observed 545 °C (Figure S21). At the onset of H_2O desorption, O removal occurs simultaneously on the surface and in the bulk, where the amount equivalent to all removable surface O is removed by 404 °C, in agreement with the experimentally determined 396 °C. The plateau observed in the experiment after the main peak is possibly due to a multimodal distribution of V_O formation energies in realistic CZO particles;³⁵ computational studies have shown that V_O formation energies depend on the local Ce/Zr distribution.^{33,36-38} TPR simulations performed with $\Delta G_{O^\circ} = 0.25$ eV results in a flatter peak at 773 °C, and a combination of spectra computed with $\Delta G_{O^\circ} = 0$ and 0.25 eV strongly resembles the experimentally observed one (Figure S22).

Although the kinetic trends observed in single-particle simulations agree with experimental observations, finer differences remain in the sub-unity order of H_2 , the slow k_{H_2O} ramp-up at 600 °C, and the slight deviation from Arrhenius-type behavior (Figure 3 and S5b). These observations may be due to the consumption of H_2 and accumulation of H_2O in the reactor, as a lower P_{H_2} and a higher P_{H_2O} both negatively affect $k_{H_2O}^p$. To examine effects beyond the kinetic limitations, we simulated the reduction of CZO in a packed bed reactor (see Section S4, Eq. S23 to S27, and Table S2). Isothermal simulations reveal that, although the reactor k_{H_2O} ($k_{H_2O}^r$) reaches its peak at the beginning of reduction at 450 and 500 °C, $k_{H_2O}^r$ grows slowly at 600 °C (Figure 5d). Indeed, while the time required to reach the maximum $k_{H_2O}^r$ (k_{max}^r) initially decreases up to ~ 500 °C due to faster $k_{H_2O}^p$ (Figure 5c,e), it sharply increases at 550 °C. Axial concentration profiles at 600 °C show that

at short times ($t \leq 10$ s), CZO at the reactor entrance quickly consumes H_2 , hindering the formation of H_2O downstream (Figure S23). When $k_{H_2O}^r$ approaches k_{max}^r ($t \sim 300$ s), the axial profile of $k_{H_2O}^p$ becomes uniform, resulting in a near-linear profile of H_2 and H_2O concentrations. This behavior contrasts from that at 500 °C: without overconsumption, $k_{H_2O}^p$ quickly becomes uniform; though, the gradual conversion of H_2 along the reactor still slows $k_{H_2O}^p$. Ultimately, reactor effects decrease E_a with increasing temperature and lower the order of H_2 (Figure S24).

Discussion

We investigated CZO reduction using a multidisciplinary approach. TPR reveals that the majority of O is removed simultaneously from the surface and the bulk of CZO particles, resulting in the major peak in the desorption spectrum. Isothermal reduction experiments reveal that the CZO reduction rate slowly diminishes after an initial maximum, consistent with simultaneous O removal, as corroborated by *in situ* Raman spectroscopy and NAP-XPS. MLP-MD simulations reveal that the pre-exponential factor and the activation energy of bulk O diffusion depend nonlinearly on temperature and degree of reduction. Further analysis of equilibrium O distributions and the correlated dynamics of V_O reveals that multiple reduction-dependent mechanisms control O diffusion. A shift from a lack of O vacancies in sparsely reduced CZO and lattice distortion in highly reduced CZO results in an optimum of bulk O mobility under relevant reaction temperatures. Finally, combined experimental and computational kinetic investigations reveal that the equilibration of O between the surface and the bulk results in a slowly diminishing reduction rate, with H_2 dissociation as the rate-limiting step. Single particle and reactor scale simulations indicate a spatially varying degree of reduction (oxidation state) of the catalyst under higher temperatures, where the kinetics is fast.

Beyond the commercial CZO sample studied in this work, the combined experimental/modeling paradigm can be extended to investigate the effects of surface structure in a single material and the redox cycling dynamics of other reducible oxides. Using CeO_2 as an example, model catalyst studies have shown that surface reducibility and the adsorption of environmental molecules depend sensitively on surface structure.³⁹ For example, H_2O and CO_2 have been shown to adsorb strongly on $CeO_2(100)$, but not as strongly on $CeO_2(111)$.^{40,41} These differences may impact the barriers and energetics of H_2 dissociation, as the initial heterolytic H-

H scission step is controlled by surface Lewis acidity/basicity, while the change in electronic energy of the overall homolytic reaction is controlled by surface reducibility.⁴² Surface acidity/basicity will also affect the degree of site-blocking due to the adsorption of product and environmental gases. Besides facet effects, the locally weakened Madelung potential at surface defects such as step edges and corners as well as in few-nm-sized particles shift the positions of the occupied and unoccupied bands,⁴³ which also result in differences in the affected sites' acid/base/redox properties and may even affect preferred reaction pathways, as demonstrated in ZrO₂.^{44,45} Finally, the random mixing of Ce and Zr cations in CZO can create locally Ce- or Zr-enriched domains and overall multimodal distributions of surface acidity, basicity, and surface/bulk reducibility.^{33,36-38} Taken together, these dependencies underscore the necessity for future work to combine experiments with strict control over sample size, shape, and composition with appropriate multiscale models for detailed investigations of redox dynamics.

Methods

Experimental Methods

Materials

Cerium zirconium oxide (CZO, 50 mol% Ce) was procured from Sigma Aldrich. H₂ (5.0), O₂ (4.7), He (5.0), and Ar (5.0) were procured from Keen Gas.

Characterization and Experiments

X-ray diffraction (XRD) patterns were measured using a Bruker D8 XRD with a Cu K α source. Average crystallite sizes were estimated using the Scherrer equation. BET surface areas were measured using N₂ at 77 K with a Micromeritics ASAP 2020 instrument. Fresh CZO samples were used as is. Pre-reduced CZO samples were reduced at 800 °C for 3 h in 100 mL/min of 10% H₂/He, then passivated in 1% O₂/N₂ at room temperature for 1 h prior to XRD or BET analyses.

Temperature programmed reduction (TPR) was done by monitoring H₂O formation with a MS. 500 mg of CZO were pelletized and sieved into 60-100 mesh particles and placed in a quartz tube using quartz wool. The TPR was conducted in a laboratory-scale reactor (Lindberg Blue M, Thermo Scientific) starting with pristine CZO and 100 mL/min of 10% H₂/He flow. All outlet lines were heated to 110 °C to avoid H₂O condensation.

Isothermal reduction was performed similarly to the TPR. 1.8 g of pristine CZO were loaded in the same tube and reactor then heated to 450-600 °C in 100 mL/min of 10% O₂/He at 10 °C/min, purged with pure He for 30 min at the target temperature, then exposed to 5-20% H₂/He. All flow rates were maintained at 100 mL/min total flow.

In situ Raman spectra were acquired in a Linkam CCR1000 stage using a HORIBA Raman Spectrometer with a green-line solid-state laser (532 nm). 40 mg of CZO or SiO₂ were pretreated in-situ with 10% O₂/Ar at 500 °C for 30 min. The samples were then purged with pure Ar then reduced in 10% H₂/Ar at 500 °C for 40 min or alternated between flows of 5.5 min of 10% H₂/Ar and 30 min of 100% Ar. All flowrates were maintained at 50 mL/min of total flow.

In situ UV-visible spectra were acquired in an in-house-built low-void-volume environmental cell using an Avantes ULS2048CL-EVO UV-vis spectrometer equipped with an AvaLight-XE light source and an adjustable UV/VIS/NIR high-temperature probe. BaSO₄ was used as a reference material for the background spectrum of the sample absorbance spectra. The CZO sample was calcined in 10% O₂/Ar for 30 min at 500 °C, purged with Ar, then reduced in 10% H₂/Ar for 30 min at 500 °C.

Near-ambient pressure X-ray photoelectron spectroscopy (NAP-XPS) spectra were collected at Brookhaven National Laboratory using a differentially pumped hemispherical analyzer (SPECS Phoibos) equipped with a monochromatic Al source (1486.6 eV). The powder sample was pressed into a thin layer onto a copper sheet. The CZO samples were pre-treated in situ with 2 mbar of O₂ at 300 °C for 20 min, then cooled to 50 °C before evacuating the chamber and repressurizing with 1 mbar of H₂. After H₂ pressure was stabilized, the CZO was heated to 500 °C at 20 °C/min, and spectra were collected every 5 min at 500 °C under 1 mbar of H₂. The XPS spectra were analyzed using CasaXPS.⁴⁶

Extent of Reduction

The extent of reduction (ζ_{red}) is defined as the fraction of removable oxygen atoms that have been removed. A maximum of 12.5% of the lattice oxygen (O_L) in CZO can be removed by reduction, defined based on the conversion of all Ce⁴⁺ to Ce³⁺. As such, ζ_{red} is equal to zero in a pristine CZO and one when 12.5% of its oxygen is removed. This fraction applies to the CZO bulk and surface.

Computational Methods

Density Functional Theory (DFT) Calculations of Bulk Ce/Zr Mixed Oxide (CZO)

All DFT calculations of CZO were performed using the Vienna ab-initio Simulation Package (VASP), version 5.4.1.⁴⁷⁻⁵⁰ The exchange-correlation energy was calculated using the Perdew-Burke-Ernzerhof (PBE) functional.⁵¹ The DFT-D3 method with the Becke-Johnson damping function (D3BJ) was used to calculate the van der Waals dispersion energy.^{52,53} Hubbard-type on-site self-interaction corrections (DFT+ U) were included using Dudarev's method,⁵⁴ where an effective value of U (U_{eff}) of 5.0 eV and 4.0 eV were applied to the Ce 4*f* and Zr 4*d* states, respectively.^{33,55,56} The core electrons were described using the projector augmented-wave method.^{57,58} In DFT calculations, a (2×2×2) supercell of the bulk CZO unit cell was used, where the Brillouin zone was sampled at the Γ point. The plane-wave kinetic energy cutoff was set to 520 eV. The electronic structure in each self-consistent field (SCF) cycle was considered converged when the difference in energies between consecutive SCF steps fell below 10⁻⁶ eV. Atomic positions in structural optimization calculations were considered converged when the Hellmann-Feynman forces on relaxed atoms fell below 0.05 eV/Å.

Construction of Machine-learning Potentials (MLPs) for Molecular Dynamics (MD) Simulations of Bulk CZO

We use the moment tensor potentials (MTPs) as part of version 2 of the MLIP software package.^{59,60} The potentials were configured using a cutoff radius of 4.5 Å and an MTP level of 12 (i.e., including all invariant moment-tensor basis functions with level ≤ 12) with 8 radial basis functions in 3 channels. Three different levels of oxide reduction were explored for training our MLP: pristine CZO, 1 oxygen vacancy (Ce_{0.5}Zr_{0.5}O_{1.97}), and 4 oxygen vacancies (Ce_{0.5}Zr_{0.5}O_{1.88}). For each level of reduction, 250 configurations were generated by randomly perturbing the structure from its relaxed geometry up to a maximum of 0.25 Å in the x , y , and z directions. This provides an initial training set for active learning with MD. Forces and energies for each structure were obtained from stationary single-point DFT calculations without geometric optimization.

The initially trained MTPs were refined through an active learning loop using MD simulations performed with the Large-scale Atomic/Molecular Massively Parallel Simulator (LAMMPS).⁶¹ The temperature was controlled using a chain of Nosé-Hoover thermostats, with a set temperature of 1800 °C and a step size of 1 fs.⁶²⁻⁶⁴ Training using the active-learning framework of the method

implemented in MLIP-2 does not use a fixed training/test split; instead, model reliability is controlled by the D-optimality extrapolation grade. For more details, see Ref ⁶⁵. For active learning, we collected structures from MD above an extrapolation grade of 2 and exited MD if the grade was above 10. DFT energies and forces were computed for new structures encountered during active learning and appended to the training set. The process continues in a loop until no structures exceed an extrapolation grade of 2 during a nanosecond-long trajectory. Finally, results of all three different levels of reduction, totaling 3635 structures, were used to train a single final MTP (see Figure S7 for accuracy and Figure S8 for sample extrapolation grades).

For the computation of oxygen self-diffusivities, we utilized the Einstein relation based on the mean squared displacement of the lattice oxygen atoms.^{66,67}

$$D \approx \frac{1}{6t} \langle |\mathbf{r}(t) - \mathbf{r}(0)|^2 \rangle \quad (1)$$

MD calculations were performed in the NVT ensemble at the desired temperature for 10 ns of equilibration, followed by 40 ns of production in the NVE ensemble (Figure S10 and S11). A larger (4×4×4) supercell was used for improved sampling.

We compute a pairwise cross-correlation function for vacancy mobility, denoted as $C_r(\tau)$, as shown in Eq. (2) A normalized form of this correlation is given in Eq. (3).

$$C_r(\tau) = \frac{1}{N_r} \sum_i \sum_{j \neq i} \langle |\mathbf{v}_i(0) \cdot \mathbf{v}_j(\tau)| \rangle_\tau \quad (2)$$

$$\tilde{C}_r(\tau) = \frac{C_r(\tau)}{\max(C_r(\tau))} \quad (3)$$

Here, N_r is the number of vacancies in the coordination shell r , \mathbf{v}_i is the velocity of vacancy i , and the assignment of distances is based on the vacancy pair separation at correlation time $\tau = 0$.

DFT Calculations of CZO Surface Reduction and Simulations of Reduction Kinetics

DFT calculations of CZO surface reduction were also performed using VASP version 5.4.1. The electronic energies were calculated using the PBE functional with the same corrections (PBE+ U +D3BJ) as stated above. One electron wavefunctions were expanded using a basis set of plane waves with kinetic energy up to 500 eV. The (111) facet of CZO was simulated using a nine-

layer-thick $p(2\times 2)$ slab, where periodic images in the z direction were separated by a 20 Å thick vacuum layer (more details are provided in Section S3 and previous work³³). The Brillouin zone was sampled at the Γ point. Unless otherwise stated, spin polarization was used in slab calculations. Dipole corrections were applied in the z direction for all slab calculations.⁶⁸ The same convergence criteria were used for the SCF cycles and structural optimizations. During structural relaxation, atoms in the bottommost tri-layer were fixed to bulk positions. Structural optimizations of transition states (TS) were performed using the climbing image nudged elastic band (CI-NEB) and quasi-Newton algorithms.^{69,70} Vibrational frequency calculations were performed using the finite difference method with a step size of 0.015 Å.

To obtain more accurate surface redox energetics for the analysis of the free energy pathways and parameterization of kinetic models, single-point calculations were performed for selected structures using the HSE06 hybrid density functional with dispersion energy calculated by the D3BJ method (more details are provided in Section S3).^{71,72} These structures were deemed important from kinetic analysis (see main text). Free energies of intermediates (IS) and TS were calculated using standard statistical mechanical equations.⁷³ Kinetic parameters for surface reactions were obtained using transition state theory (TST), while those for adsorption steps were calculated using collision theory.⁷⁴ The multiscale kinetics of CZO reduction were evaluated at both the single-particle and the reactor scale (more details are provided in Section S4).

Data Availability

Additional data to support the findings of this study are provided in the Supplementary Information. Source data are provided with this paper. Further data are available from the corresponding author upon request.

References

- 1 Montini, T., Melchionna, M., Monai, M. & Fornasiero, P. Fundamentals and Catalytic Applications of CeO₂-Based Materials. *Chem. Rev.* **116**, 5987-6041 (2016).
- 2 Gorte, R. J. Ceria in catalysis: From automotive applications to the water–gas shift reaction. *AIChE J.* **56**, 1126-1135 (2010).

- 3 Vivier, L. & Duprez, D. Ceria-Based Solid Catalysts for Organic Chemistry. *ChemSusChem* **3**, 654-678 (2010).
- 4 McIntosh, S. & Gorte, R. J. Direct Hydrocarbon Solid Oxide Fuel Cells. *Chem. Rev.* **104**, 4845-4866 (2004).
- 5 Chueh, W. C. *et al.* High-Flux Solar-Driven Thermochemical Dissociation of CO₂ and H₂O Using Nonstoichiometric Ceria. *Science* **330**, 1797-1801 (2010).
- 6 Serra, J. M. *et al.* Hydrogen production via microwave-induced water splitting at low temperature. *Nat. Energy* **5**, 910-919 (2020).
- 7 Wang, C. *et al.* Green Syngas Production by Microwave-Assisted Dry Reforming of Methane on Doped Ceria Catalysts. *ACS Sustainable Chem. Eng.* **11**, 13353-13362 (2023).
- 8 Vannice, M. A. An analysis of the Mars–van Krevelen rate expression. *Catal. Today* **123**, 18-22 (2007).
- 9 Hwang, A., Wu, J., Getsoian, A. B. & Iglesia, E. Kinetic Relevance of Surface Reactions and Lattice Diffusion in the Dynamics of Ce–Zr Oxides Reduction–Oxidation Cycles. *J. Phys. Chem. C* **127**, 2936-2952 (2023).
- 10 Hwang, A., Getsoian, A. B. & Iglesia, E. Kinetics, Mechanism, and Thermodynamics of Ceria-Zirconia Reduction. *ACS Catal.* **14**, 16184-16204 (2024).
- 11 Holmgren, A., Duprez, D. & Andersson, B. A Model of Oxygen Transport in Pt/Ceria Catalysts from Isotope Exchange. *J. Catal.* **182**, 441-448 (1999).
- 12 Vasiliades, M. A. *et al.* Deciphering the role of nano-CeO₂ morphology on the dry reforming of methane over Ni/CeO₂ using transient and isotopic techniques. *Appl. Catal. B: Environ. Energy* **350**, 123906 (2024).
- 13 Wang, Y.-G., Mei, D., Li, J. & Rousseau, R. DFT+U Study on the Localized Electronic States and Their Potential Role During H₂O Dissociation and CO Oxidation Processes on CeO₂(111) Surface. *J. Phys. Chem. C* **117**, 23082-23089 (2013).
- 14 Sun, L., Marrocchelli, D. & Yildiz, B. Edge dislocation slows down oxide ion diffusion in doped CeO₂ by segregation of charged defects. *Nat. Commun.* **6**, 6294 (2015).
- 15 Zhang, D., Han, Z.-K., Murgida, G. E., Ganduglia-Pirovano, M. V. & Gao, Y. Oxygen-Vacancy Dynamics and Entanglement with Polaron Hopping at the Reduced CeO₂(111) Surface. *Phys. Rev. Lett.* **122**, 096101 (2019).
- 16 Zhang, Y. *et al.* Revealing the Non-Arrhenius Migration of Oxygen Vacancies at the CeO₂(111) Surface. *J. Phys. Chem. Lett.* **16**, 3734-3740 (2025).
- 17 Paier, J., Penschke, C. & Sauer, J. Oxygen defects and surface chemistry of ceria: quantum chemical studies compared to experiment. *Chem. Rev.* **113**, 3949-3985 (2013).
- 18 Sauer, J. The future of computational catalysis. *J. Catal.* **433**, 115482 (2024).
- 19 Yao, H. C. & Yao, Y. F. Y. Ceria in automotive exhaust catalysts: I. Oxygen storage. *J. Catal.* **86**, 254-265 (1984).

- 20 Schilling, C. & Hess, C. Real-Time Observation of the Defect Dynamics in Working Au/CeO₂ Catalysts by Combined Operando Raman/UV–Vis Spectroscopy. *J. Phys. Chem. C* **122**, 2909-2917 (2018).
- 21 Weber, W. H., Hass, K. C. & McBride, J. R. Raman study of $\{\mathrm{CeO}\}_2$: Second-order scattering, lattice dynamics, and particle-size effects. *Phys. Rev. B* **48**, 178-185 (1993).
- 22 Loridant, S. Raman spectroscopy as a powerful tool to characterize ceria-based catalysts. *Catal. Today* **373**, 98-111 (2021).
- 23 Mosca, S. *et al.* Spatially Offset Raman Spectroscopy—How Deep? *Anal. Chem.* **93**, 6755-6762 (2021).
- 24 Song, J. *et al.* Penetration depth at various Raman excitation wavelengths and stress model for Raman spectrum in biaxially-strained Si. *Sci. China Phys. Mech. Astron.* **56**, 2065-2070 (2013).
- 25 Borowicz, P. Depth-Sensitive Raman Investigation of Metal-Oxide-Semiconductor Structures: Absorption as a Tool for Variation of Exciting Light Penetration Depth. *J. Spectrosc.* **2016**, 1617063 (2016).
- 26 Bañares, M. A. Operando methodology: combination of in situ spectroscopy and simultaneous activity measurements under catalytic reaction conditions. *Catal. Today* **100**, 71-77 (2005).
- 27 Patil, B. S., Srinivasan, P. D., Atchison, E., Zhu, H. & Bravo-Suárez, J. J. Design, modelling, and application of a low void-volume in situ diffuse reflectance spectroscopic reaction cell for transient catalytic studies. *React. Chem. Eng.* **4**, 667-678 (2019).
- 28 Moncada, J., Adams, W. R., Thakur, R., Julin, M. & Carrero, C. A. Developing a Raman Spectrokinetic Approach To Gain Insights into the Structure–Reactivity Relationship of Supported Metal Oxide Catalysts. *ACS Catal.* **8**, 8976-8986 (2018).
- 29 Lee, J. *et al.* How Pt Influences H₂ Reactions on High Surface-Area Pt/CeO₂ Powder Catalyst Surfaces. *JACS Au* **3**, 2299-2313 (2023).
- 30 Kato, S. *et al.* Quantitative depth profiling of Ce³⁺ in Pt/CeO₂ by in situ high-energy XPS in a hydrogen atmosphere. *Phys. Chem. Chem. Phys.* **17**, 5078-5083 (2015).
- 31 Duchoň, T. *et al.* Ordered phases of reduced ceria as epitaxial films on Cu(111). *J. Phys. Chem. C* **118**, 357-365 (2013).
- 32 Hwang, A., Wu, J., Getsoian, A. B. & Iglesia, E. Non-Equilibrium Thermodynamic Treatments of Lattice Diffusion Dynamics in Ceria-Zirconia and Related Redox-Active Oxides. *J. Phys. Chem. C* **129**, 19772-19785 (2025).
- 33 Srinivas, S., Yan, G., Caratzoulas, S. & Vlachos, D. G. Vacancy formation, stability, and electronic properties of nickel on equimolar ceria–zirconia mixed oxide (111) catalyst. *Catal. Sci. & Technol.* **15**, 3412-3422 (2025).
- 34 Cohen, M. & Vlachos, D. G. Modified Energy Span Analysis Reveals Heterogeneous Catalytic Kinetics. *Ind. Eng. Chem. Res.* **61**, 5117-5128 (2022).
- 35 Daturi, M. *et al.* Reduction of High Surface Area CeO₂–ZrO₂ Mixed Oxides. *J. Phys. Chem. B* **104**, 9186-9194 (2000).

- 36 Wang, H.-F. *et al.* A Model to Understand the Oxygen Vacancy Formation in Zr-Doped CeO₂: Electrostatic Interaction and Structural Relaxation. *J. Phys. Chem. C* **113**, 10229-10232 (2009).
- 37 Wang, H.-F., Guo, Y.-L., Lu, G.-Z. & Hu, P. Maximizing the Localized Relaxation: The Origin of the Outstanding Oxygen Storage Capacity of κ -Ce₂Zr₂O₈. *Angew. Chem. Int. Ed.* **48**, 8289-8292 (2009).
- 38 Otero, G. S., Lustemberg, P. G., Prado, F. & Ganduglia-Pirovano, M. V. Relative Stability of Near-Surface Oxygen Vacancies at the CeO₂(111) Surface upon Zirconium Doping. *J. Phys. Chem. C* **124**, 625-638 (2020).
- 39 Mullins, D. R. The surface chemistry of cerium oxide. *Surf. Sci. Rep.* **70**, 42-85 (2015).
- 40 Mullins, D. R. *et al.* Water dissociation on CeO₂(100) and CeO₂(111) thin films. *J. Phys. Chem. C* **116**, 19419-19428 (2012).
- 41 Albrecht, P. M., Jiang, D.-e. & Mullins, D. R. CO₂ Adsorption As a Flat-Lying, Tridentate Carbonate on CeO₂(100). *J. Phys. Chem. C* **118**, 9042-9050 (2014).
- 42 Abdelgaid, M. & Mpourmpakis, G. Structure–Activity Relationships in Lewis Acid–Base Heterogeneous Catalysis. *ACS Catal.* **12**, 4268-4289 (2022).
- 43 Pacchioni, G. & Freund, H.-J. Controlling the charge state of supported nanoparticles in catalysis: lessons from model systems. *Chem. Soc. Rev.* **47**, 8474-8502 (2018).
- 44 Ruiz Puigdollers, A., Tosoni, S. & Pacchioni, G. Turning a Nonreducible into a Reducible Oxide via Nanostructuring: Opposite Behavior of Bulk ZrO₂ and ZrO₂ Nanoparticles Toward H₂ Adsorption. *J. Phys. Chem. C* **120**, 15329-15337 (2016).
- 45 Ruiz Puigdollers, A., Illas, F. & Pacchioni, G. Reduction of Hydrogenated ZrO₂ Nanoparticles by Water Desorption. *ACS Omega* **2**, 3878-3885 (2017).
- 46 Fairley, N. *et al.* Systematic and collaborative approach to problem solving using X-ray photoelectron spectroscopy. *Appl. Surf. Sci. Adv.* **5**, 100112 (2021).
- 47 Kresse, G. & Hafner, J. Ab initio molecular dynamics for liquid metals. *Phys. Rev. B* **47**, 558-561 (1993).
- 48 Kresse, G. & Hafner, J. Ab initio molecular-dynamics simulation of the liquid-metal--amorphous-semiconductor transition in germanium. *Phys. Rev. B* **49**, 14251-14269 (1994).
- 49 Kresse, G. & Furthmüller, J. Efficient iterative schemes for ab initio total-energy calculations using a plane-wave basis set. *Phys. Rev. B* **54**, 11169-11186 (1996).
- 50 Kresse, G. & Furthmüller, J. Efficiency of ab-initio total energy calculations for metals and semiconductors using a plane-wave basis set. *Comput. Mater. Sci.* **6**, 15-50 (1996).
- 51 Perdew, J. P., Burke, K. & Ernzerhof, M. Generalized gradient approximation made simple. *Phys. Rev. Lett.* **77**, 3865-3868 (1996).
- 52 Grimme, S., Antony, J., Ehrlich, S. & Krieg, H. A consistent and accurate ab initio parametrization of density functional dispersion correction (DFT-D) for the 94 elements H-Pu. *J. Chem. Phys.* **132**, 154104 (2010).
- 53 Grimme, S., Ehrlich, S. & Goerigk, L. Effect of the damping function in dispersion corrected density functional theory. *J. Comput. Chem.* **32**, 1456-1465 (2011).

- 54 Dudarev, S. L., Botton, G. A., Savrasov, S. Y., Humphreys, C. J. & Sutton, A. P. Electron-energy-loss spectra and the structural stability of nickel oxide: an LSDA+U study. *Phys. Rev. B* **57**, 1505-1509 (1999).
- 55 Zhang, C., Michaelides, A., King, D. A. & Jenkins, S. J. Anchoring Sites for Initial Au Nucleation on CeO₂{111}: O Vacancy versus Ce Vacancy. *J. Phys. Chem. C* **113**, 6411-6417 (2009).
- 56 Chen, H.-Y. T., Tosoni, S. & Pacchioni, G. Adsorption of Ruthenium Atoms and Clusters on Anatase TiO₂ and Tetragonal ZrO₂(101) Surfaces: A Comparative DFT Study. *J. Phys. Chem. C* **119**, 10856-10868 (2015).
- 57 Blöchl, P. E. Projector augmented-wave method. *Phys. Rev. B* **50**, 17953-17979 (1994).
- 58 Kresse, G. & Joubert, D. From ultrasoft pseudopotentials to the projector augmented-wave method. *Phys. Rev. B* **59**, 1758-1775 (1999).
- 59 Shapeev, A. V. Moment Tensor Potentials: A Class of Systematically Improvable Interatomic Potentials. *Multiscale Model. Simul.* **14**, 1153-1173 (2016).
- 60 Novikov, I. S., Gubaev, K., Podryabinkin, E. V. & Shapeev, A. V. The MLIP package: moment tensor potentials with MPI and active learning. *Mach. Learn.: Sci. Technol.* **2**, 025002 (2021).
- 61 Thompson, A. P. *et al.* LAMMPS - a flexible simulation tool for particle-based materials modeling at the atomic, meso, and continuum scales. *Comput. Phys. Commun.* **271**, 108171 (2022).
- 62 Nosé, S. A unified formulation of the constant temperature molecular dynamics methods. *J. Chem. Phys.* **81**, 511-519 (1984).
- 63 Hoover, W. G. Canonical dynamics: Equilibrium phase-space distributions. *Phys. Rev. A* **31**, 1695-1697 (1985).
- 64 Martyna, G. J., Klein, M. L. & Tuckerman, M. Nosé–Hoover chains: The canonical ensemble via continuous dynamics. *J. Chem. Phys.* **97**, 2635-2643 (1992).
- 65 Podryabinkin, E. V. & Shapeev, A. V. Active learning of linearly parametrized interatomic potentials. *Comput. Mater. Sci.* **140**, 171-180 (2017).
- 66 Michaud-Agrawal, N., Denning, E. J., Woolf, T. B. & Beckstein, O. MDAAnalysis: A toolkit for the analysis of molecular dynamics simulations. *J. Comput. Chem.* **32**, 2319-2327 (2011).
- 67 Gowers, R. J. *et al.* MDAAnalysis: a Python package for the rapid analysis of molecular dynamics simulations. Report No. 2575-9752, (Los Alamos National Laboratory (LANL), Los Alamos, NM (United States), 2019).
- 68 Neugebauer, J. & Scheffler, M. Adsorbate-substrate and adsorbate-adsorbate interactions of Na and K adlayers on Al(111). *Phys. Rev. B* **46**, 16067-16080 (1992).
- 69 Henkelman, G., Uberuaga, B. P. & Jonsson, H. A climbing image nudged elastic band method for finding saddle points and minimum energy paths. *J. Chem. Phys.* **113**, 9901-9904 (2000).

- 70 Henkelman, G. & Jónsson, H. Improved tangent estimate in the nudged elastic band method for finding minimum energy paths and saddle points. *J. Chem. Phys.* **113**, 9978-9985 (2000).
- 71 Heyd, J., Scuseria, G. E. & Ernzerhof, M. Hybrid functionals based on a screened Coulomb potential. *J. Chem. Phys.* **118**, 8207-8215 (2003).
- 72 Heyd, J., Scuseria, G. E. & Ernzerhof, M. Erratum: “Hybrid functionals based on a screened Coulomb potential” [*J. Chem. Phys.* 118, 8207 (2003)]. *J. Chem. Phys.* **124**, 219906 (2006).
- 73 Hill, T. L. *An introduction to statistical thermodynamics*. 1-544 (Courier Corporation, 1986).
- 74 Wittreich, G. R., Alexopoulos, K. & Vlachos, D. G. Microkinetic modeling of surface catalysis. *Handbook of Materials Modeling: Applications: Current and Emerging Materials*, 1377-1404 (2020).

Acknowledgements

This work was supported by the Basic Energy Sciences, Office of Science, under award number DE-SC0024085 (D.G.V.). Research was carried out in part at the Center for Functional Nanomaterials at Brookhaven National Laboratory, supported by the U.S. Department of Energy, Office of Basic Energy Sciences, under Contract No. DE-SC0012704. S. Sourav acknowledges the New Faculty Scheme (NFSc), Indian Institute of Technology Madras-IP24250561CHNFSC009141 (S. Sourav). This research was also partly supported by the high-performance computing resources of the Information Technologies (IT) at the University of Delaware.

Author contributions

D.G.V. and W.Z. supervised the project. Q.K. conducted all the experiments. S.Y. and J.A.B. assisted with the NAP-XPS, and S. Sourav assisted with the Raman experiments. S. Srinivas and G.Y. performed DFT calculations of CZO slabs. G.Y. carried out the kinetic simulations. A.W. performed DFT calculations of bulk CZO, trained the MLPs, and carried out the MD simulations. The manuscript was principally prepared by Q.K., G.Y., A.W., S. Srinivas, and D.G.V., with feedback from other authors. All authors contributed to the discussion of the results.

Competing interests statement

There are no competing interests to declare.

Figures and figure legends/captions

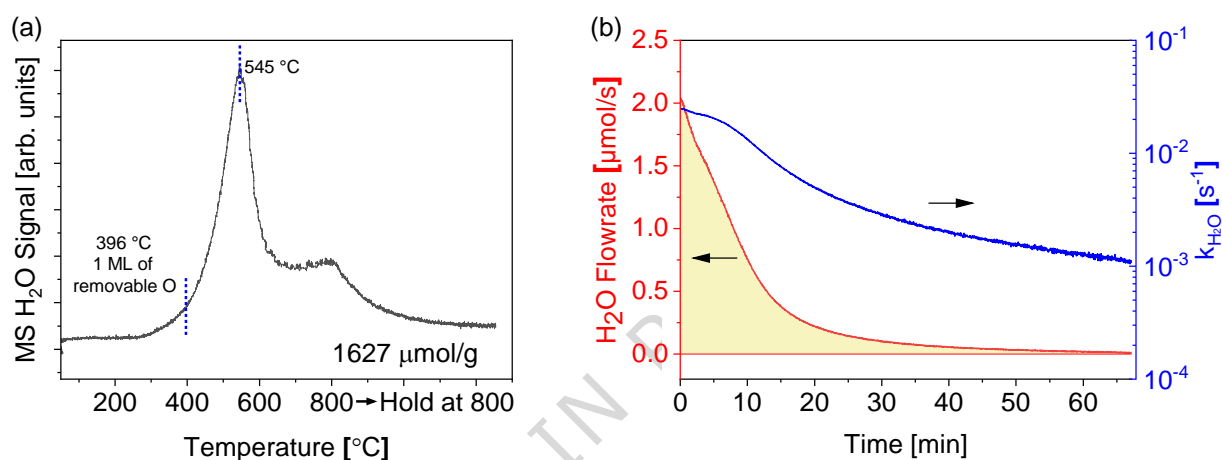


Figure 1. Transient and isothermal reduction kinetics using online mass spectrometry. (a) H₂-TPR of CZO in 100 mL/min of 10% H₂/He at 10 °C/min. One monolayer (ML) of removable O is removed by 396 °C. (b) H₂O formation at 500 °C during reduction in 100 mL/min of 10% H₂/He flow.

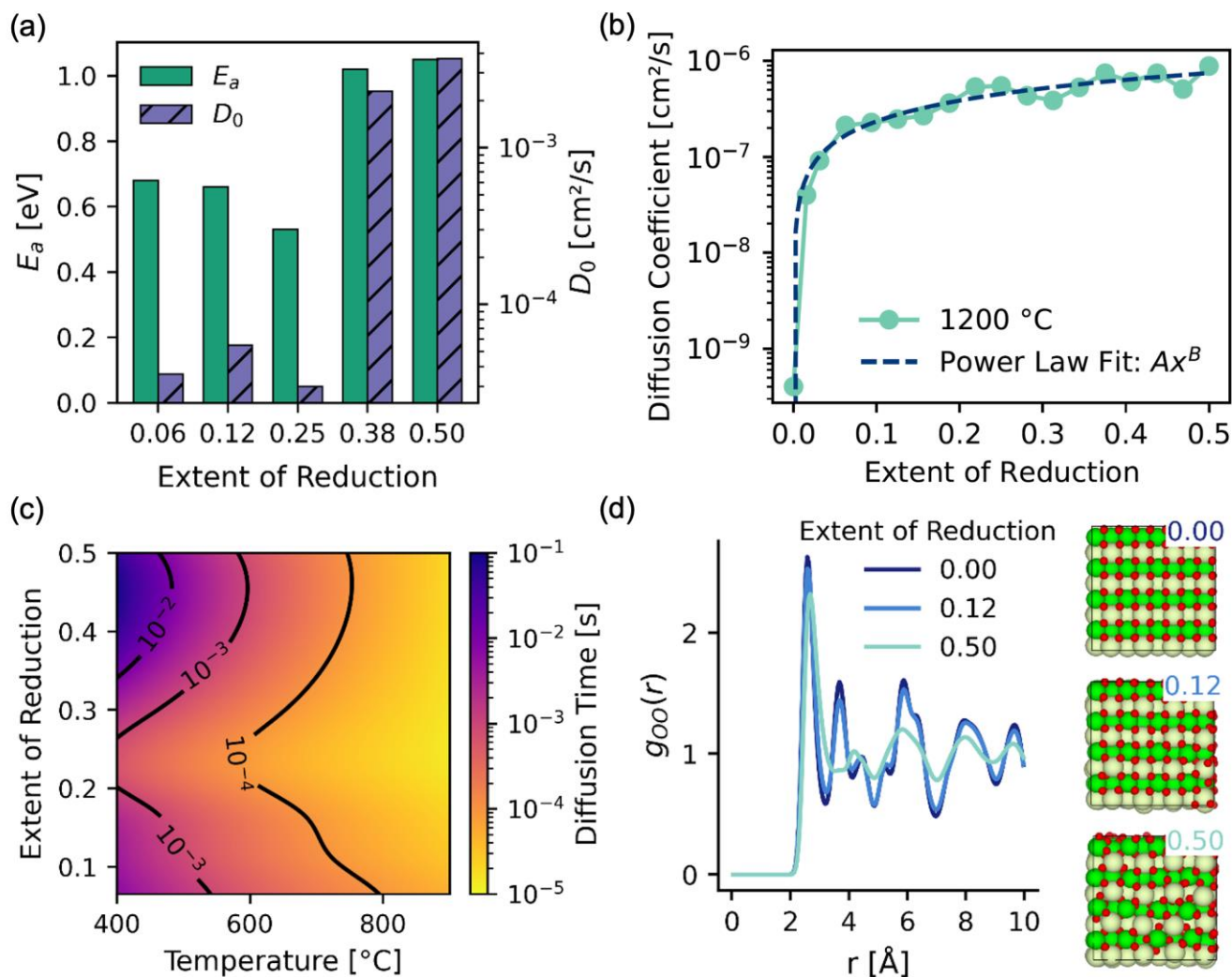


Figure 2: Bulk oxygen mobility obtained and crystal distortion from multiscale DFT-MLP-MD simulations. (a) Pre-exponential factors (D_0) and activation energies (E_a) obtained from Arrhenius fits over the temperature range of 1100–1500 °C for reductions ranging from $\text{Ce}_{0.5}\text{Zr}_{0.5}\text{O}_{1.99}$ to $\text{Ce}_{0.5}\text{Zr}_{0.5}\text{O}_{1.88}$. (b) Oxygen diffusivity as a function of oxygen vacancy concentration at 1200 °C ($A = 1.2 \times 10^{-6} \text{ cm}^2/\text{s}$, $B = 0.72$). (c) Heat map of the diffusion time scale vs. temperature and vacancy concentration. (d) Oxygen-oxygen radial distribution function (g_{OO}) at 1200 °C for three vacancy concentrations showing the distortion of oxygen coordination at higher vacancy concentrations.

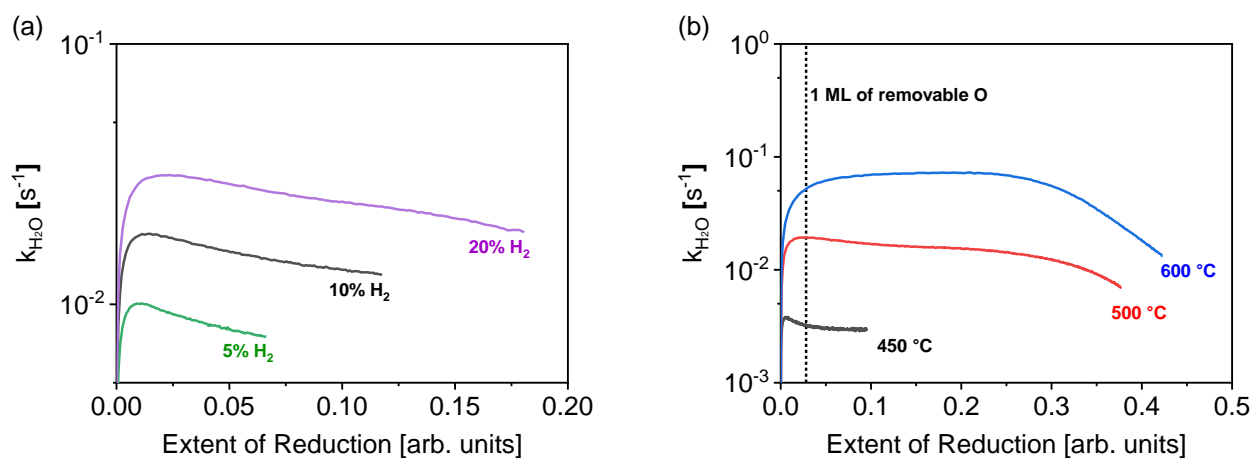


Figure 3. Time on stream kinetics at various H₂ partial pressures and temperatures. (a) Normalized rate of H₂O formation (k_{H_2O}) during reduction in 5, 10, and 20% H₂/He. (b) k_{H_2O} during reduction in 10% H₂/He at 450, 500, and 600 °C. The dotted line marks where one monolayer (ML) of removable O has been removed.

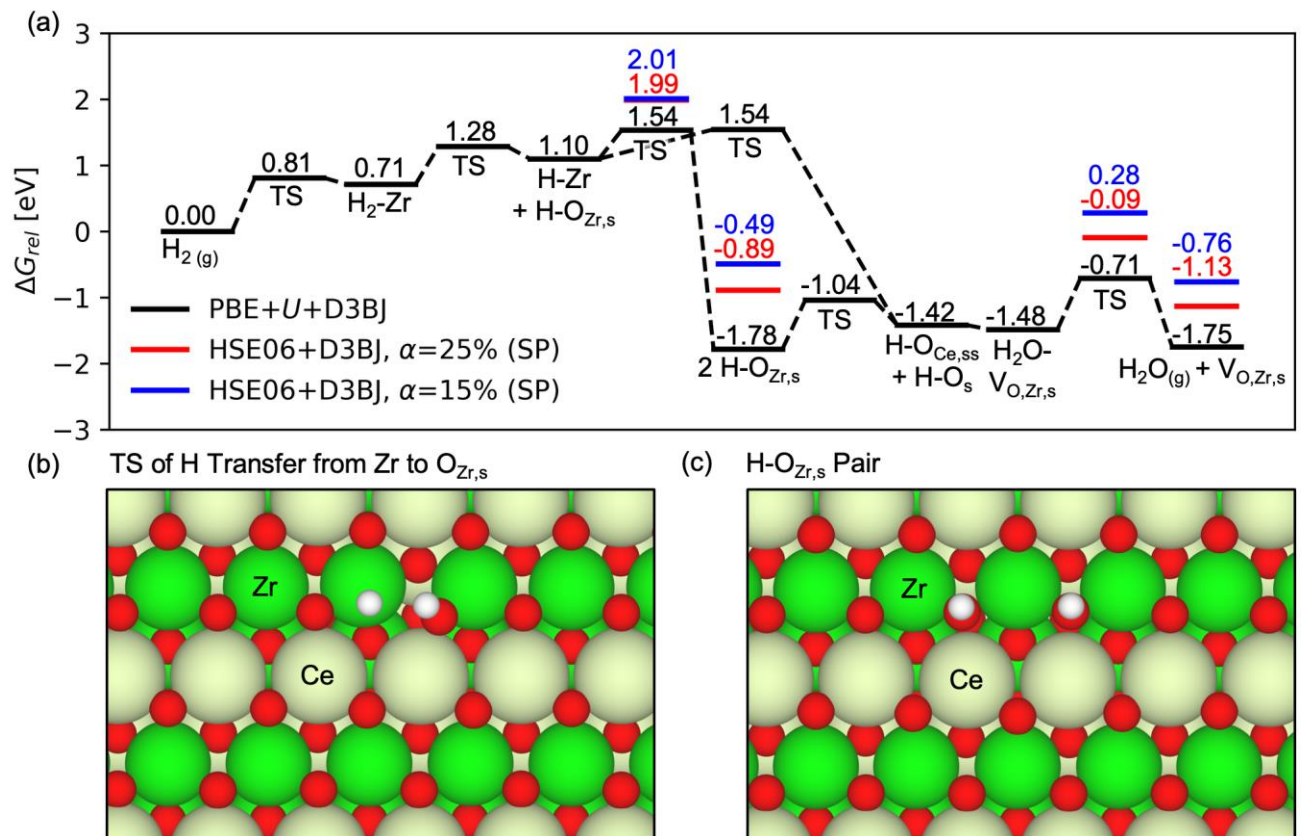


Figure 4. Mechanism of the reduction of CZO by H_2 . (a) Pressure-corrected free energy (ΔG_{rel}) pathway of the initial reduction of the (111) facet of CZO by H_2 , evaluated at $T = 500$ °C, $P_{H_2} = 10^{-1}$ atm, and $P_{H_2O} = 10^{-2}$ atm. Free energies of intermediates and transition states calculated at the PBE+*U*+D3BJ level are shown in black, while those of kinetically relevant states calculated using single-point (SP) calculations at the HSE06+D3BJ level are shown in red and blue, corresponding to the use of 25% and 15% exact exchange (α), respectively. (b) Geometry of the transition state (TS) of H transfer from Zr to $O_{Zr,s}$. (c) Geometry of a pair of H- $O_{Zr,s}$ groups produced by the TS shown in (b).

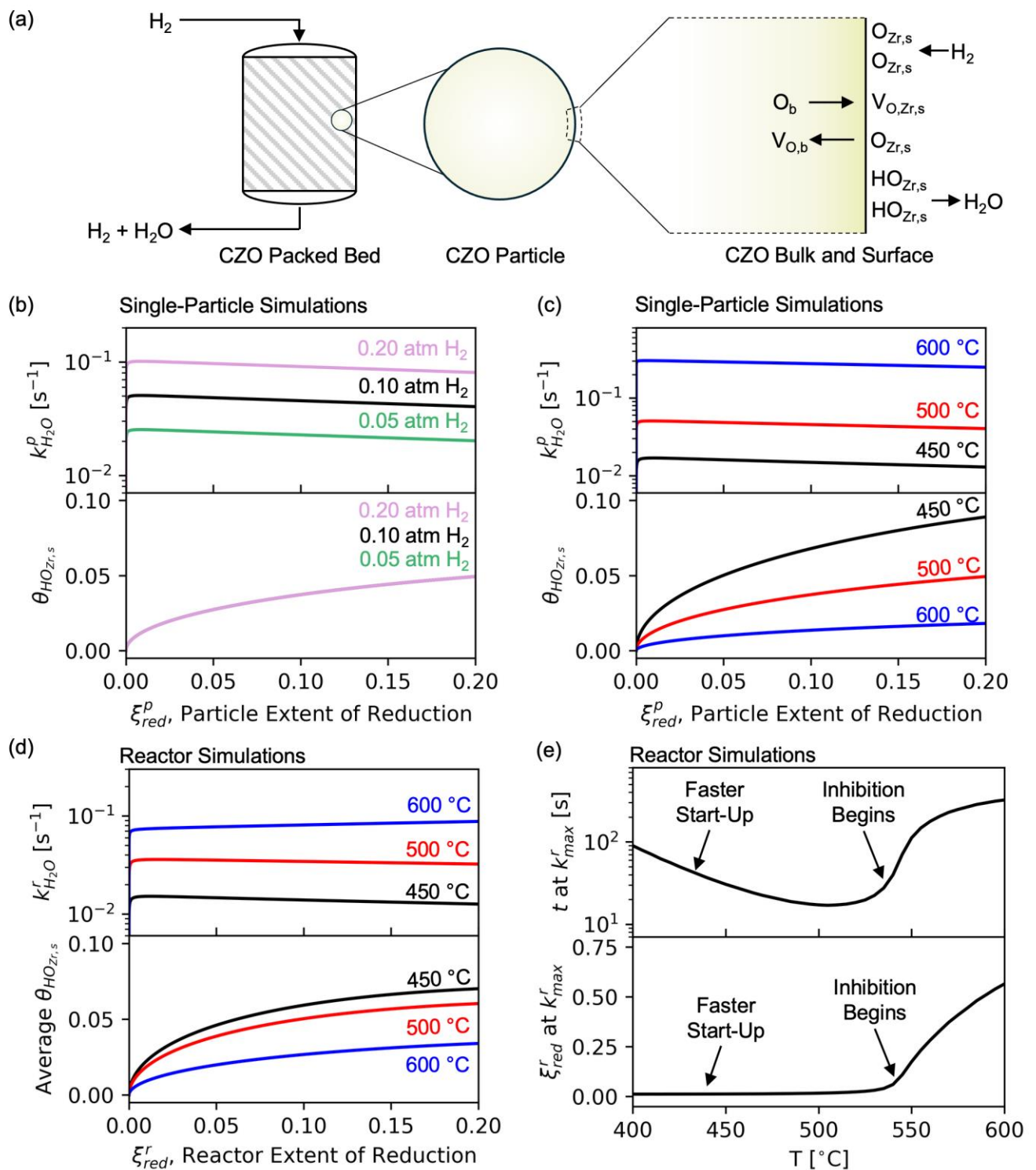


Figure 5. Multiscale kinetic models of CZO reduction. (a) Schematic of the multiscale model. (b) Isothermal reduction kinetics of a single 32 nm CZO particle vs. its extent of reduction (ξ_{red}^p). Dependence of the single-particle normalized rate of H_2O formation ($k_{H_2O}^p$) and the coverage of $HO_{Zr,s}$ groups ($\theta_{HO_{Zr,s}}$) on the partial pressure of H_2 (P_{H_2}) at 500 °C with the partial pressure of

H₂O (P_{H_2O}) set to 10^{-2} atm. (c) Dependence of $k_{H_2O}^p$ and $\theta_{HOZr,s}$ on temperature, with $P_{H_2} = 10^{-1}$ atm and $P_{H_2O} = 10^{-2}$ atm. (d) Isothermal reduction kinetics of 32 nm CZO particles in a packed bed reactor. Dependence of the reactor normalized rate of H₂O formation ($k_{H_2O}^r$) and reactor-averaged $\theta_{HOZr,s}$ on temperature with inlet $P_{H_2} = 10^{-1}$ atm and flow rate set to 100 mL/min. (e) Time required to reach the maximum $k_{H_2O}^r$ (k_{max}^r) and the reactor extent of reduction (ξ_{red}^r) at k_{max}^r vs. temperature.

Supplementary information

Additional details and results of kinetic and spectroscopic experiments, MD simulations, DFT calculations, and kinetic simulations. (pdf)

ARTICLE IN PRESS

Editorial summary: The interplay between bulk oxygen diffusion and surface reactions in reducible metal oxides is key in heterogeneous catalysts, yet direct measurements of their coupling through transient kinetics and in situ spectroscopies have been lacking. Here, the authors uncover complex H₂-driven dynamics in ceria–zirconia using transient mass spectrometry along with in-situ Raman, near-ambient pressure X-ray photoelectron spectroscopy, machine learning potential-based molecular simulations, and multiscale kinetic modeling.

Peer review information: *Nature Communications* thanks the anonymous reviewers for their contribution to the peer review of this work. A peer review file is available.

ARTICLE IN PRESS